

Effects of Midlevel Dry Air on Development of the Axisymmetric Tropical Cyclone Secondary Circulation

JOSHUA J. ALLAND, BRIAN H. TANG, AND KRISTEN L. CORBOSIERO

*Department of Atmospheric and Environmental Sciences, University at Albany,
State University of New York, Albany, New York*

(Manuscript received 23 September 2016, in final form 1 February 2017)

ABSTRACT

Idealized experiments conducted with an axisymmetric tropical cyclone (TC) model are used to assess the effects of midlevel dry air on the axisymmetric TC secondary circulation. Moist entropy diagnostics of convective parcels are used to determine how midlevel dry air affects the distribution and strength of convection. Analyzing upward and downward motions in the Eulerian radius–height coordinate system shows that the moistest simulation has stronger vertical motions and a wider overturning circulation compared to drier simulations. A Lagrangian entropy framework further analyzes convective motions by separating upward higher-entropy streams from downward lower-entropy streams. Results show that the driest simulation has a weaker mean overturning circulation with updrafts characterized by lower mean entropy compared to moister simulations. Turbulent entrainment of dry air into deep convection at midlevels is small, suggesting that the influence of midlevel dry air on convective strength and the structure of the secondary circulation are through modification of the inflow layer. Backward trajectories show low-entropy air subsiding into the subcloud layer from low to midlevels of the atmosphere between radii of 200 and 400 km. Surface fluxes increase the entropy of these parcels before they rise in convective updrafts, but the increased recovery time, combined with descending motion closer to the inner core, decreases the width of the TC secondary circulation in the driest simulation.

1. Introduction

The tropics are generally characterized by a midlevel minimum in (moist) entropy (Jordan 1958; Ooyama 1969; Dunion 2011), which is an important limitation on tropical cyclone (TC) development (Emanuel 1989). Moistening the troposphere is necessary prior to TC formation (Rotunno and Emanuel 1987; Nolan et al. 2007; Rappin et al. 2010; Raymond et al. 2011; Smith and Montgomery 2012; Tang and Emanuel 2012b; Wang 2012, 2014; Zawislak and Zipser 2014; Rios-Berrios et al. 2016) and may be an important discriminator between developing and nondeveloping systems (Davis and Ahijevych 2012; Smith and Montgomery 2012; Komaromi 2013). Some studies suggest that moistening the free troposphere to near saturation, through cumulus congestus detrainment (Wang 2014), suppresses convective downdrafts, allowing surface fluxes to increase the entropy in the subcloud layer and, through convective adjustment, the temperature of the troposphere. This temperature

increase is associated with an amplification of the warm core and low-level vortex (Rotunno and Emanuel 1987; Emanuel 1995; Raymond 1995; Bister and Emanuel 1997; Raymond et al. 1998). On the contrary, other studies suggest that midlevel moistening does not necessarily suppress convective downdrafts but, instead, promotes stronger updrafts by reducing dry-air entrainment into convective plumes (Nolan 2007; James and Markowski 2010; Smith and Montgomery 2012; Wang 2012). Once the midtroposphere approaches saturation, deep convection increases and the low-level vortex intensifies.

Dry midlevel air also affects TC intensification. Tang and Emanuel (2010) discuss two pathways by which midlevel low-entropy air can reduce the strength of convection and inhibit TC intensification. The first is a low-level pathway and involves the transport of dry air into the subcloud layer from convective downdrafts (Barnes et al. 1983; Powell 1990; Kimball 2006; Hince and Houze 2008; Didlake and Houze 2009; Riemer et al. 2010; Molinari et al. 2013; Riemer et al. 2013; Riemer and Laliberté 2015). This low-entropy air is then

Corresponding author e-mail: Joshua J. Alland, jalland@albany.edu

DOI: 10.1175/JAS-D-16-0271.1

© 2017 American Meteorological Society. For information regarding reuse of this content and general copyright information, consult the [AMS Copyright Policy](http://www.ametsoc.org/PUBSReuseLicenses) (www.ametsoc.org/PUBSReuseLicenses).

TABLE 1. Parameterization schemes used in the ASPECH model.

	Parameterization
Radiation	Newtonian relaxation (Rotunno and Emanuel 1987)
Microphysics	Kessler (Kessler 1969)
Turbulence	Bryan (2008) , but with fully compressible equations
Surface fluxes	Bulk aerodynamic formulas (Donelan et al. 2004 ; Black et al. 2007 ; Haus et al. 2010)

transported inward by the radial flow and can lower the azimuthal mean entropy of the eyewall ([Braun et al. 2012](#); [Ge et al. 2013](#)). The lower mean entropy of the eyewall leads to shallower convection, less latent heat release in middle to upper levels, and a hydrostatic pressure rise in the eye ([Powell 1990](#)). From an energetics perspective, TC weakening occurs if the flux of low-entropy air from midlevels is comparable to the surface entropy flux, because the mechanical energy generated from surface fluxes cannot compensate for both the intrusion of low-entropy air and frictional dissipation ([Tang and Emanuel 2010](#)). The second pathway describes the direct ventilation of dry environmental air into the eyewall through turbulent entrainment ([Brown and Zhang 1997](#); [Frank and Ritchie 2001](#); [Emanuel et al. 2004](#); [Cram et al. 2007](#); [Shelton and Molinari 2009](#)), lowering the mean entropy of the eyewall. This pathway also leads to shallower convection and less latent heat release in the middle to upper levels of the atmosphere. The two pathways disrupt the hurricane heat engine ([Simpson and Riehl 1958](#)) because the mid- to low-level ventilation is located where the entropy difference between the TC inner core and the environment is typically the greatest ([Tang and Emanuel 2012a](#)).

Dry air can also affect TC size. Past modeling studies have shown that a moist environment produces larger storms compared to dry environments ([Kimball 2006](#); [Hill and Lackmann 2009](#); [Wang 2009](#); [Xu and Wang 2010](#); [Braun et al. 2012](#)). These findings were associated with increased rainband activity in a moister environment. Increased heating in the region of rainband activity increases cyclonic potential vorticity at low levels and extends the areal extent of the circulation. A drier environment decreases precipitation in outer rainbands, resulting in a smaller TC ([Matyas and Cartaya 2009](#); [Ying and Zhang 2012](#)).

[Tang et al. \(2016\)](#) used an axisymmetric model to investigate the sensitivity of TC development to the initial midlevel moisture above the subcloud layer, from a saturated to a very dry free troposphere. As the initial free troposphere became drier, the upward vertical mass flux decreased and the envelope of deep convection narrowed, resulting in a longer TC spinup time. From their study, questions were raised regarding how dry air impacts deep convection and the secondary circulation. For example, does dry air decrease the vertical mass flux

through lateral entrainment directly into convection or vertically through subsidence and/or turbulent mixing into the inflow layer? Additionally, how does dry air affect the structure of the developing TC secondary circulation? For example, does dry air control the radial location of convection, which in turn impacts the evolution of the secondary circulation?

The goal of this study is to address the questions above by investigating how midlevel dry air impacts convection and the development of the secondary circulation through the idealized simulations used in [Tang et al. \(2016\)](#). [Section 2](#) discusses the model setup and initial conditions. [Section 3](#) documents the evolution of the simulated TCs and convective motions in physical geometry using an Eulerian analysis. Additionally, [section 3](#) presents a complimentary Lagrangian analysis that shows the bulk convective upward and downward motions of the secondary circulation. [Section 4](#) uses forward and backward trajectories to determine the source region of dry air documented in [section 3](#). [Section 5](#) concludes with the main findings of this study.

2. Methodology

a. Axisymmetric model setup

This study utilizes the Axisymmetric Simplified Pseudoadiabatic Entropy Conserving Hurricane (ASPECH) model ([Tang and Emanuel 2012a](#)). The details of the model setup are described in [Tang et al. \(2016\)](#) and are summarized as follows. The model is nonhydrostatic, compressible, and phrased in cylindrical coordinates on an f plane. The Coriolis parameter is set to $5 \times 10^{-5} \text{ s}^{-1}$. The radial grid spacing is 2 km and the vertical grid spacing is 0.3 km. A simple set of parameterization schemes are employed and are listed in [Table 1](#). Note that a simple warm-rain microphysics scheme is used.

ASPECH uses (moist) entropy s as its prognostic thermodynamic variable. The entropy in the ASPECH model is expressed as

$$s = c_{pd} \log \theta + \frac{L_v q}{T_L} - R_d \log p_o, \quad (1)$$

where c_{pd} is the specific heat of dry air at constant pressure, θ is the potential temperature, L_v is the latent heat of vaporization, q is the water vapor mixing ratio,

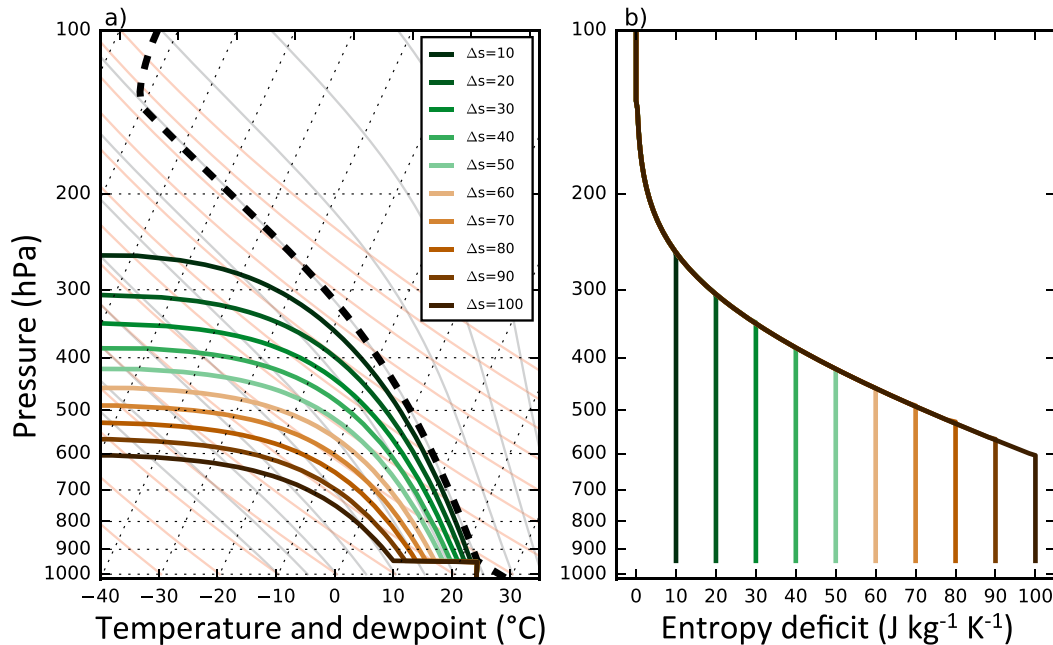


FIG. 1. (a) Initial skew T - $\log p$ soundings for each experimental set. Temperature is given by the dashed black line. Dewpoint is given by the solid colored lines. (b) Entropy deficit profiles corresponding to the soundings in (a). Adapted from Tang et al. (2016).

T_L is the saturation temperature, R_d is the gas constant of dry air, and p_o is the reference pressure.

A major benefit of the ASPECH model is that the entropy is materially conserved in the absence of internal and boundary sources and sinks, such as surface fluxes, turbulent mixing, and radiation. This benefit allows for a precise accounting of entropy and the characteristics of convection for different initial moisture environments.

b. Initial conditions

As was discussed in our previous paper (Tang et al. 2016), the initial conditions of the experiments are as follows. Ten sets of experiments were conducted. All experiments have a moist neutral temperature profile, relative to a subcloud-layer parcel, up to the tropopause at 135 hPa. Each experiment also has the same subcloud-layer water vapor mixing ratio of 19 g kg^{-1} and a sea surface temperature (SST) of 30°C . This SST is 1°C greater than the initial surface air temperature, which was motivated by observed values in the tropics (Fairall et al. 1996).

The radial structure of the initial vortex is specified using Eq. (6) from Knaff et al. (2011), with a radius of maximum wind of 100 km, a radius of zero wind of 500 km, and a maximum tangential wind of 15 m s^{-1} . The vortex decays with height, vanishing above 15 km. The temperature is then adjusted to be in thermal wind

balance with the vortex, adapted from the procedure of Smith (2006).

The 10 experimental sets differ in the initial moisture profile. This study uses the nondimensional entropy deficit (Emanuel 2010) χ to specify the initial moisture above the subcloud layer:

$$\chi = \frac{s_m^* - s_m}{s_{\text{SST}}^* - s_b}, \quad (2)$$

where s_m , s_m^* , s_{SST}^* , and s_b are the entropy at midlevels, the saturation entropy at midlevels, the saturation entropy at the sea surface, and the entropy of the subcloud layer, respectively. The numerator is the entropy deficit Δs above the subcloud layer and increases as the relative humidity decreases (Emanuel et al. 2008). The denominator is a measure of the air–sea disequilibrium. Each experimental set has a different mixing ratio profile above the initial lifting condensation level (Fig. 1a), corresponding to a fixed entropy deficit in the numerator of Eq. (2) (Fig. 1b). Note that the denominator of Eq. (2) is initially the same across experiments. The sets are incremented by an entropy deficit of $10 \text{ J kg}^{-1} \text{ K}^{-1}$, ranging from near saturation ($\Delta s = 10 \text{ J kg}^{-1} \text{ K}^{-1}$) to the driest profile ($\Delta s = 100 \text{ J kg}^{-1} \text{ K}^{-1}$).

Each experimental set has 20 ensemble members, generated by adding uniformly distributed, random perturbations to the initial water vapor mixing ratio in

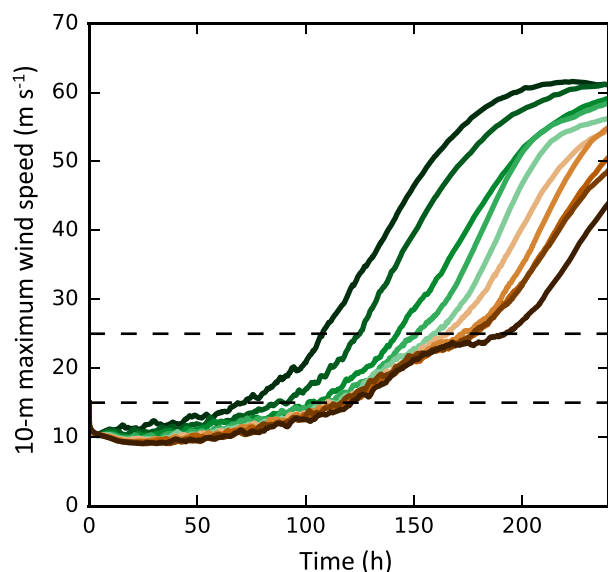


FIG. 2. Time series of the ensemble-mean 10-m maximum wind speed (m s^{-1}) for each experimental set from Fig. 1. Colors for each set are as in Fig. 1. The dashed horizontal black lines at 15 and 25 m s^{-1} represent the end of the preconditioning and spinup periods, respectively. Adapted from Tang et al. (2016).

the lowest three model levels, similar to the methodology of Van Sang et al. (2008). The perturbations have a maximum amplitude of 1 g kg^{-1} , a mean of zero, and are different for each experiment.

Figure 2 shows the evolution of the ensemble-mean 10-m maximum wind speed for each experimental set. At the beginning of each experiment, the boundary layer develops and the initial low-level vortex decays because of frictional dissipation. After this initial decay, all experiments have a period of slow intensification (called the preconditioning period) followed by a period of faster intensification (called the spinup period). We define the end of the preconditioning and spinup periods as when the 10-m maximum wind speed first returns to 15 m s^{-1} and when it reaches 25 m s^{-1} , respectively. Although criteria for these times are arbitrary, they represent a consistent basis for comparison between experiments based on intensity.

Figure 3 shows the ensemble-mean 10-m wind profile for each experimental set averaged during the final 12 h of the preconditioning (Fig. 3a) and spinup (Fig. 3b) periods. The 10-m wind speed radially outward of 200 km at a given radius generally decreases as the initial entropy deficit increases. The differences arise during the preconditioning period and persist during the spinup period for all radii greater than the radius of maximum wind. These results suggest that the initial entropy deficit plays a role in the size of the developing low-level circulation in these experiments.

For simplicity, most of the remaining content describes the evolution of convection and its effect on the secondary circulation between experimental sets with entropy deficits of 10 and $100 \text{ J kg}^{-1} \text{ K}^{-1}$. These experiments represent the evolution of the simulated TCs from a very moist ($\Delta s = 10 \text{ J kg}^{-1} \text{ K}^{-1}$) to a very dry ($\Delta s = 100 \text{ J kg}^{-1} \text{ K}^{-1}$) initial free troposphere, and are called the moist and dry simulations, respectively. The next section compares the entropy and secondary circulation in the moist and dry simulations during the preconditioning and spinup periods.

3. Evolution of entropy and the secondary circulation

We will investigate the evolution of the secondary circulation in the moist and dry simulations through three complementary methods: a traditional Eulerian approach (height–radius space), a new Lagrangian approach (height–entropy space) documented in Pauluis and Mrowiec (2013), and forward and backward trajectories. The former two methods allow for a macroscopic view of the secondary circulation and processes that control the entropy along the secondary circulation, while the last method reveals the dominant physical pathway by which low-entropy air enters the circulation in physical space.

a. Eulerian perspective

Figures 4a and 4c show the ensemble-mean entropy and radial wind for the two experimental sets averaged during the final 12 h of the preconditioning period. The moist simulation reaches the end of the preconditioning period about 40 h faster than the dry simulation, as seen in Fig. 2. The radial inflow is slightly stronger in the moist simulation, with inflow magnitudes greater than 2 m s^{-1} extending to a radius of 400 km. The radial outflow structure at upper levels has greater differences, with the moist simulation having outflow that extends beyond 800 km. The entropy distributions also vary considerably between simulations. The moist simulation has a large radial width of vertically deep entropy values above $2600 \text{ J kg}^{-1} \text{ K}^{-1}$, associated with deep convection. In contrast, the dry simulation has a narrower radial width of high-entropy values. In fact, low-entropy air of less than $2550 \text{ J kg}^{-1} \text{ K}^{-1}$ extends down from midlevels into the top of the radial inflow layer around 400 km in the dry simulation.

The entropy and radial wind differences between simulations continue during the final 12 h of the spinup period (Figs. 4b and 4d). The radial inflow and outflow in the moist simulation extend to a larger radius compared to the dry simulation. A vertically deep column of high

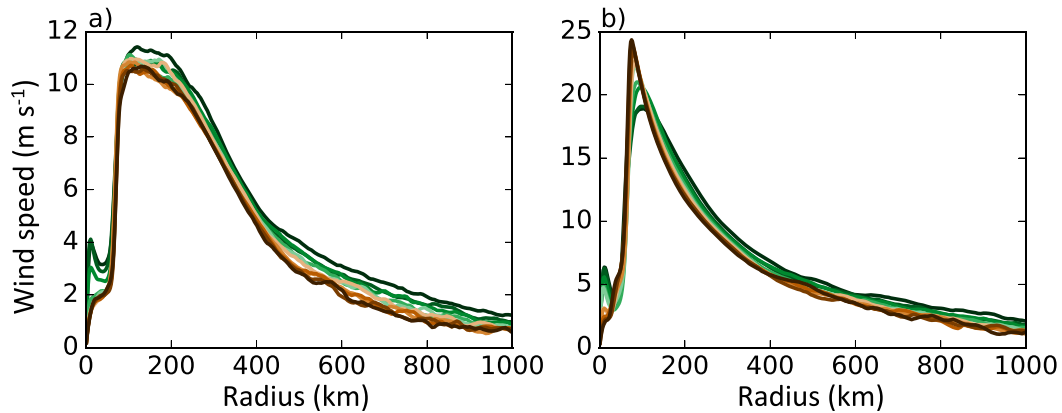


FIG. 3. Ensemble-mean radial profile of the 10-m wind (m s^{-1}) for each experimental set in Fig. 1. The profiles are averaged over the (a) preconditioning and (b) spinup periods and extend for the final 12 h of the respective period. Colors for each set are as in Fig. 1.

entropy, associated with coherent deep convection, becomes more defined in both simulations. While both the moist and dry simulations have increased entropy in this column compared to the preconditioning period, it extends over a narrower radial width in the dry simulation, and the low-entropy air at midlevels still appears to intrude into the top of the radial inflow layer, this time around 300 km.

The entropy and radial wind differences between simulations during the preconditioning and spinup periods suggest differences in convection. Figure 5 shows the distribution of updrafts and the Eulerian streamfunction time averaged over the final 12 h of the preconditioning (Figs. 5a and 5c) and spinup (Figs. 5b and 5d) periods. The shading represents the frequency of exceedance of vertical motion greater

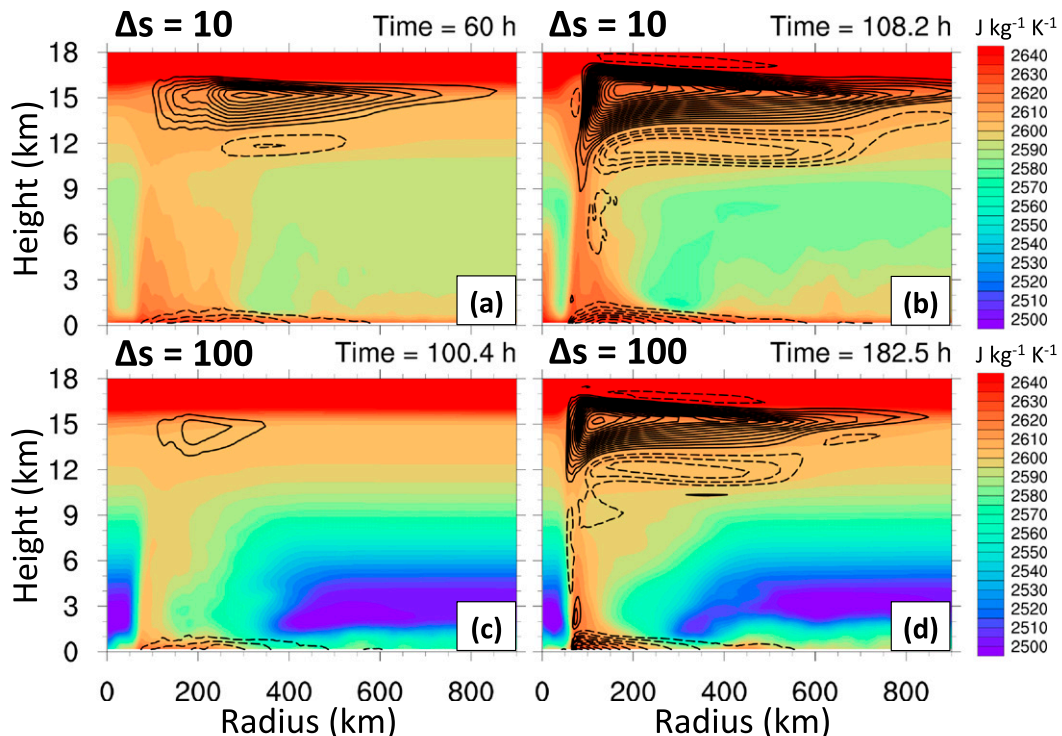


FIG. 4. Ensemble-mean entropy (shaded) and radial wind (contoured every 1 m s^{-1}) with an initial Δs of (a),(b) 10 and (c),(d) $100 \text{ J kg}^{-1} \text{ K}^{-1}$ during the final 12 h of the (a),(c) preconditioning and (b),(d) spinup periods. Solid and dashed lines represent positive and negative radial wind, respectively. The times at the end of the preconditioning and spinup periods are given above the top-right corner of each panel.

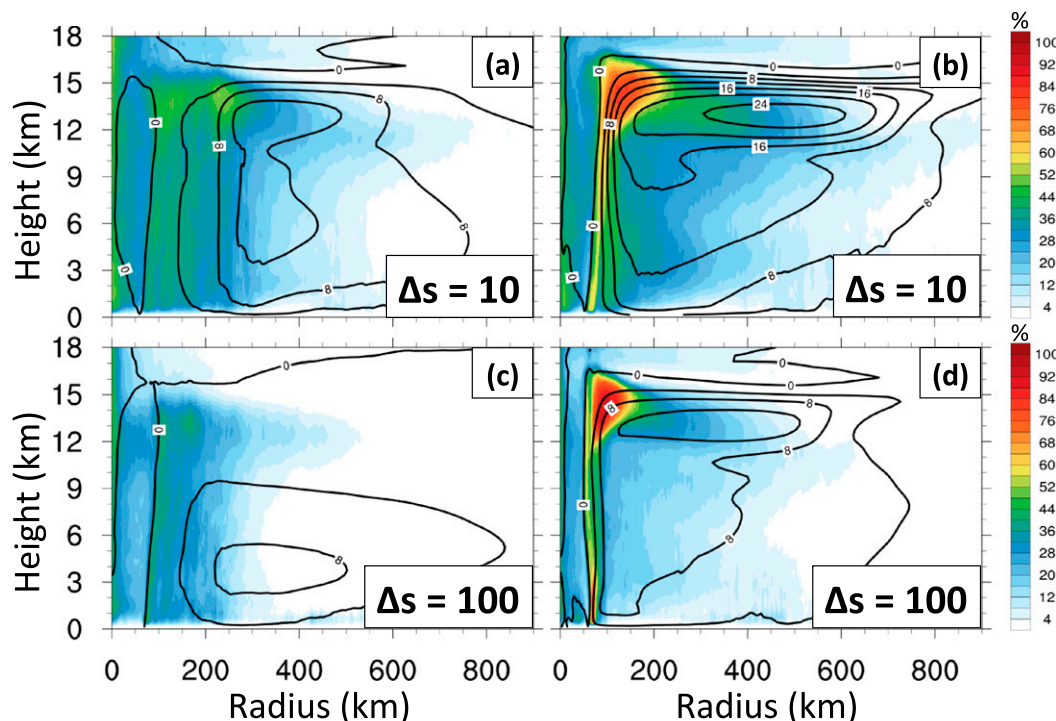


FIG. 5. Ensemble-mean, time-averaged frequency of vertical motion greater than 0.05 m s^{-1} (shaded) and Eulerian streamfunction (contoured every $4 \times 10^8 \text{ kg s}^{-1}$) with an initial Δs of (a),(b) 10 and (c),(d) $100 \text{ J kg}^{-1} \text{ K}^{-1}$. The time average is over the (a),(c) preconditioning and (b),(d) spinup periods and extends for the final 12 h of the respective period.

than 0.05 m s^{-1} over the 12 h period. The Eulerian streamfunction ψ is defined as

$$\psi = \int_0^z -u\rho_d r dz', \quad (3)$$

where u is the radial wind, ρ_d is the density of dry air, and r is radius. The Eulerian streamfunction gives a measure of the strength and width of the secondary circulation.

During the preconditioning period (Figs. 5a and 5c), the moist simulation has the higher frequency of vertical motion greater than 0.05 m s^{-1} encompassing the inner 300 km and extending over the depth of the troposphere. The streamfunction supports what is seen in the updraft distribution, with the upward branch of the vertically deep secondary circulation aligned with the highest frequency of upward motion. In the dry simulation during the preconditioning period, vertical motion greater than 0.05 m s^{-1} is less frequent and more radially confined to the inner 200 km. The Eulerian streamfunction is weaker than the moist simulation and the overturning circulation is shallower. This result is consistent with shallower convection and a lower detrainment height in the dry simulation (Tang et al. 2016).

During the spinup period (Figs. 5b and 5d), the moist simulation has a much stronger vertically deep secondary circulation, and the frequency of vertical motion greater than 0.05 m s^{-1} increases substantially for radii between 50 and 100 km. The streamfunction shows a stronger, wider secondary circulation has developed. Once deep convection is established in the dry simulation during the spinup period, the radial distribution of frequent upward motion is more confined compared to the moist simulation. As a result, the streamfunction in the dry simulation is weaker and narrower. The radial differences in the updraft distribution between simulations are consistent with the entropy distribution in Fig. 4, where the dry simulation has a narrower radial width of high entropy.

Dry air has the potential to increase downdraft frequency and strength by enhancing evaporative cooling. Figures 6a and 6c show the distribution of downward motion as a frequency of vertical motion less than -0.05 m s^{-1} during the preconditioning period. The moist simulation has downward motion overlapping the region of upward motion in Fig. 5a. Frequencies greater than 28% at low levels extend to roughly 300 km. The dry simulation has a narrower radial width of downward motion at low levels, with frequencies greater than 28%

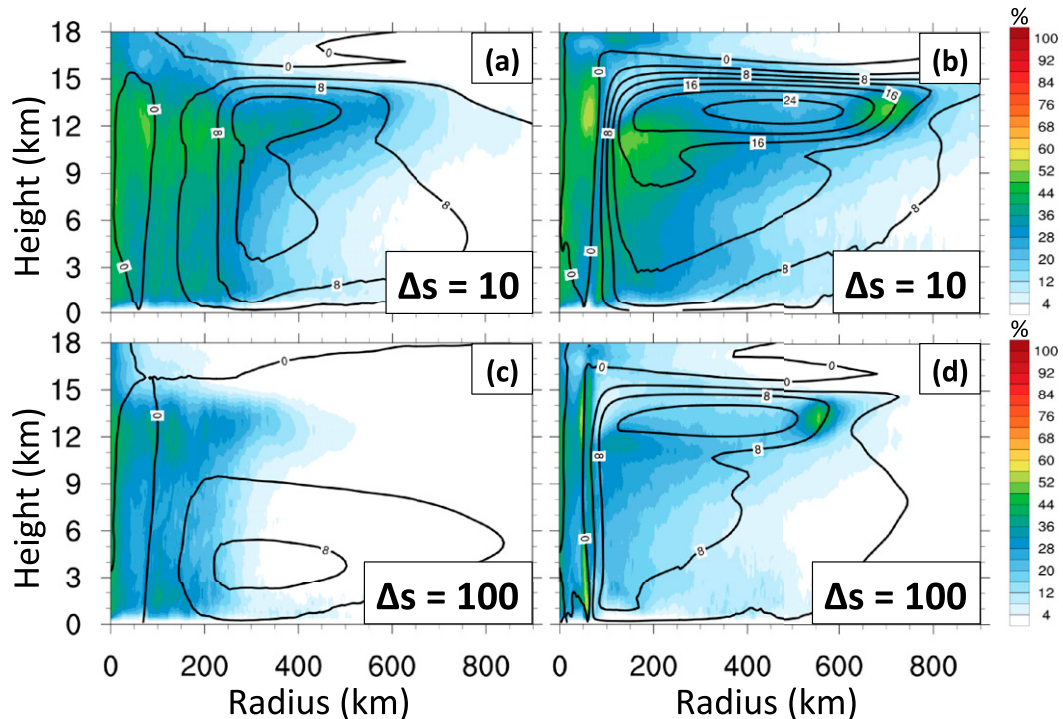


FIG. 6. As in Fig. 5, but for the ensemble-mean, time-averaged frequency of vertical motion less than -0.05 m s^{-1} .

mainly within the inner 200 km. Downdrafts do not appear to be more frequent in the dry simulation. These results agree with James and Markowski (2010), who show that a moister environment produces convection with both stronger upward and downward motions.

During the spinup period (Figs. 6b and 6d), downward motion flanks the location of upward motion (Figs. 5b and 5d), with the moist simulation having higher frequencies in both the inner 300 km and for most vertical levels. The downward branch of the secondary circulation is noticeable in the upper troposphere at outer radii for both simulations. The greatest frequency of downward motion extends from roughly 650 to 800 km and from 500 to 600 km in the moist and dry simulations, respectively.

The variation of the secondary circulation strength and size with initial entropy deficit is confirmed in Fig. 7 for all experimental sets averaged over the spinup period. Figure 7a shows a decrease in the ensemble-mean streamfunction maximum with increasing initial entropy deficit. Additionally, Fig. 7b shows a decrease in the ensemble-mean radial location of the maximum frequency of downward motion outside a radius of 400 km, representing the downward branch of the secondary circulation, with increasing initial entropy deficit. These results are consistent with a decrease in the vertical mass flux with increasing initial entropy deficit (Tang et al. 2016) and confirm the relationship between the initial entropy deficit and the structure of the secondary circulation.

Low-entropy air decreases the frequency of both upward and downward motions and reduces the strength and radial extent of the secondary circulation. However, because upward and downward motions occupy the same Eulerian space in a statistical sense, it is difficult to diagnose the effect of midlevel low-entropy air on net upward and downward motions. To better diagnose the effect of low-entropy air on these motions, we turn to a Lagrangian entropy framework.

b. Lagrangian perspective

Convective motions are analyzed using a Lagrangian approach developed in Pauluis and Mrowiec (2013) and utilized to study mass transport in hurricanes in Mrowiec et al. (2016). This framework takes advantage of the material conservation of entropy in ASPECH, allowing one to systematically track the thermodynamic evolution of parcels. Additionally, this framework separates vertical mass transport in terms of entropy, effectively partitioning higher-entropy upward motion from lower-entropy downward motion. This partitioning allows one to characterize upward and downward motions more cleanly, simplifying the interpretation of complex convective motions. Pauluis et al. (2008, 2010) used a similar technique to investigate the mean meridional global circulation.

Pauluis and Mrowiec (2013) and Mrowiec et al. (2016) define an operator, using angle brackets, on a variable f

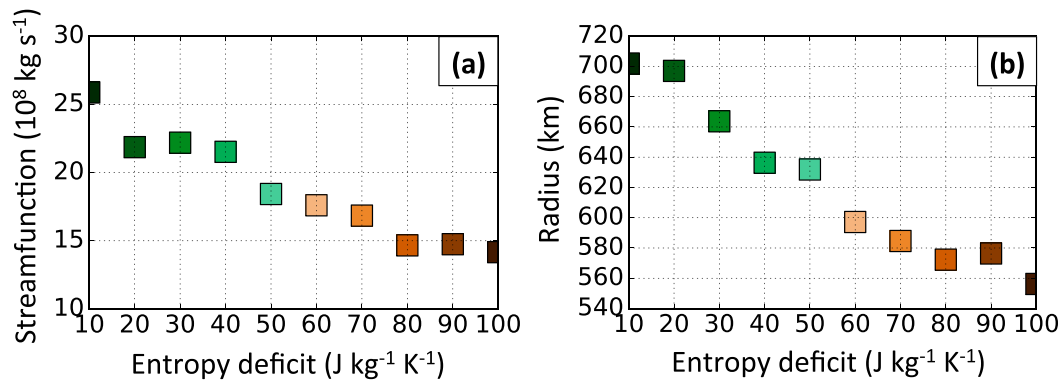


FIG. 7. Ensemble-mean (a) Eulerian streamfunction maximum and (b) radius of the maximum frequency of downward motion (outside 400 km) for each experimental set averaged over the spinup period. Each radius was determined by finding the maximum frequency associated with the downward branch of the secondary circulation in Figs. 6b and 6d, but for all experimental sets.

in an entropy–height coordinate system, which is modified here for the cylindrical coordinate system of the ASPECH model as

$$\langle f \rangle(z, s_0) = \frac{2\pi}{P} \int_0^P \int_0^R f(r, z, t) \delta[s_0 - s(r, z, t)] r dr dt, \quad (4)$$

where s is the entropy, P is the time period of averaging, R is the radius of the outer domain (1500 km), δ is a Dirac delta function, and s_0 is the integration entropy. Equation (4) effectively bins parcels by entropy and can be used to study the mean thermodynamic properties of upward and downward motions, to the extent to which these motions are separated in entropy space.

The isentropic mean of a variable is given as

$$\langle \tilde{f} \rangle(z, s) = \frac{\langle \rho_d f \rangle(z, s)}{\langle \rho_d \rangle(z, s)}, \quad (5)$$

where $\langle \tilde{f} \rangle$ is the isentropic mean of f at a given height and entropy and $\langle \rho_d \rangle$ is the isentropic-mean density of dry air. The isentropic analysis is similar between

ensemble members from each respective experimental set, so an arbitrary run is chosen in the moist and dry experiments to compare. Figures 8a and 8b display the isentropic-mean values of water vapor mixing ratio for a single run in the moist and dry simulations, respectively, averaged during the final 12 h of the preconditioning period. These figures show the range of water vapor mixing ratio at each vertical level. Both simulations have high water vapor mixing ratios near the surface that decrease with height. The dry simulation has a larger range of water vapor mixing ratio values at midlevels, from very moist in convection to near zero in the environment.

The goal of utilizing the entropy framework is to diagnose the effect low-entropy midlevel air has on convective upward and downward motions. The vertical mass flux in the entropy framework defines an isentropic mean overturning circulation, where the ascent of warm moist air is balanced by the descent of cool dry air (Pauluis and Mrowiec 2013). Equation (4) is used to define the Lagrangian mean overturning circulation in terms of the vertical mass flux (Mrowiec et al. 2016):

$$\langle \rho w \rangle(z, s_0) = \frac{2\pi}{P} \int_0^P \int_{R_1}^{R_2} \rho [w(r, z, t) - \bar{w}(z, t)] \delta[s_0 - s(r, z, t)] r dr dt, \quad (6)$$

where the mean vertical velocity \bar{w} in the domain bounded by radii R_1 and R_2 is removed. Subtracting out the mean vertical velocity allows one to define a closed isentropic streamfunction Ψ given as

$$\Psi(z, s) = \int_{-\infty}^s \langle \rho w \rangle(z, s') ds', \quad (7)$$

where s' is a dummy variable. Both the isentropic-mean vertical mass flux and streamfunction represent

the mean overturning circulation in the Lagrangian framework.

Figures 9a and 9c show the isentropic-mean vertical mass flux and streamfunction of a single run for the full domain of the moist and dry simulations during the final 12 h of the preconditioning period. Warm and cool colors represent upward and downward motions, respectively, and parcels move parallel to the isentropic streamfunction contours, effectively separating

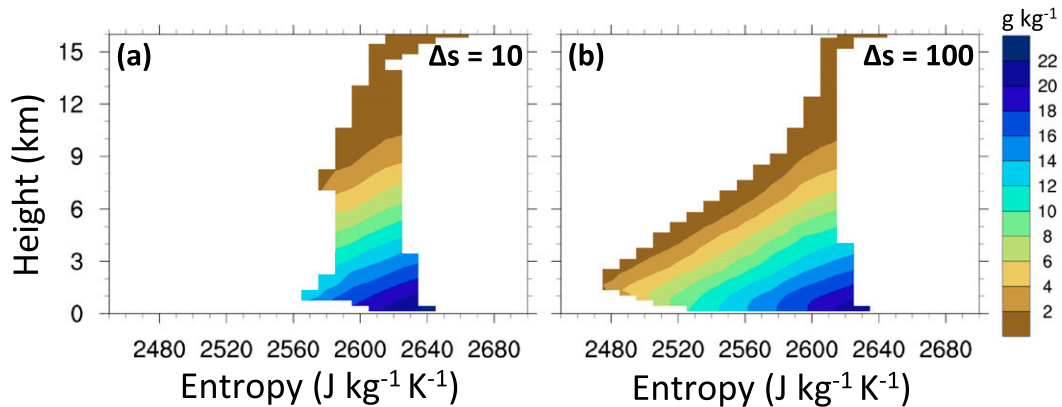


FIG. 8. Time-averaged, isentropic-mean water vapor mixing ratio (g kg^{-1}) for a single run with an initial Δs of (a) 10 and (b) $100 \text{ J kg}^{-1} \text{ K}^{-1}$. The time average extends for the final 12 h of the preconditioning period.

upward high-entropy streams from downward low-entropy streams.

The moist simulation has a deep, strong secondary circulation that extends over the depth of the troposphere during the preconditioning period (Fig. 9a). The rising stream has entropy values between 2610 and $2640 \text{ J kg}^{-1} \text{ K}^{-1}$ at low levels, slightly decreasing with height by about $10 \text{ J kg}^{-1} \text{ K}^{-1}$. The descending stream has lower entropy values than the upward stream, between 2580 and $2610 \text{ J kg}^{-1} \text{ K}^{-1}$, and follows the average

entropy profile with descent. A second overturning circulation that closes between 4 and 7 km is also evident, but the ascending and descending branches largely overlap with the tropospheric deep circulation.

Two overturning circulations are also apparent in the dry simulation (Fig. 9c). The first overturning circulation has a rising stream with entropy values at low levels between 2600 and $2630 \text{ J kg}^{-1} \text{ K}^{-1}$, a shift to lower entropy compared to the moist simulation. The entropy and vertical mass flux of this rising stream decrease by

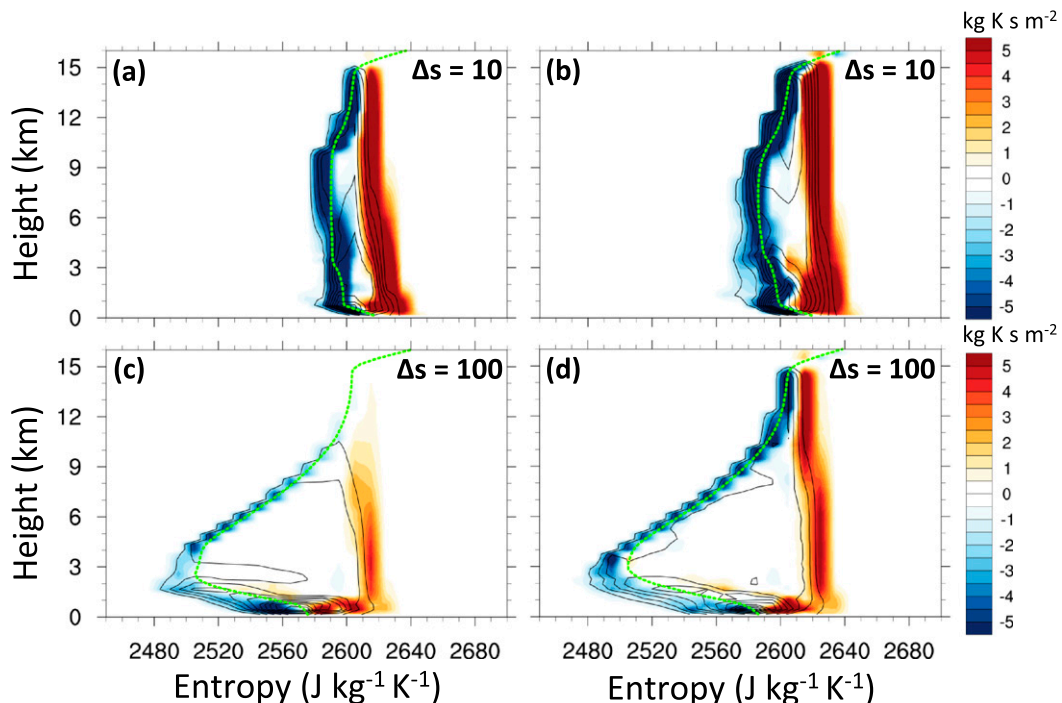


FIG. 9. Time-averaged, isentropic vertical mass flux (shaded, $\times 10^8 \text{ kg K s m}^{-2}$) and streamfunction (contoured every $2 \times 10^9 \text{ kg s}^{-1}$) for a single run with an initial Δs of (a),(b) 10 and (c),(d) $100 \text{ J kg}^{-1} \text{ K}^{-1}$ during the (a),(c) preconditioning and (b),(d) spinup periods. The green dotted line represents the mean entropy profile. The time average extends for the final 12 h of the respective period.

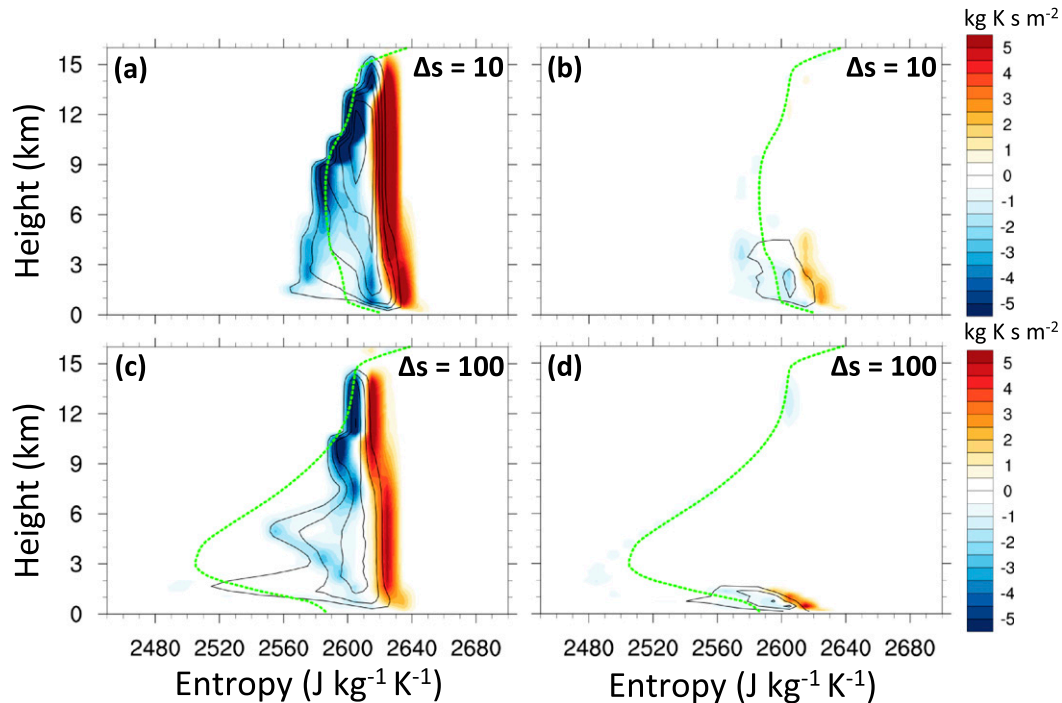


FIG. 10. As in Fig. 9, except during the spinup period for (a),(c) the inner 300 km and (b),(d) radii between 300 and 600 km.

about $10 \text{ J kg}^{-1} \text{ K}^{-1}$ with height, similar to the moist simulation. The streamfunction closes around 9 km, suggesting detrainment at and below this level as convective parcels lose buoyancy through mixing with environment air. The descending stream generally follows the average entropy profile, which decreases from 9 to 3 km as a result of radiational cooling. A second overturning circulation exists at low levels from the surface to 2 km. This circulation has a rising stream with entropy values between 2575 and $2610 \text{ J kg}^{-1} \text{ K}^{-1}$ that decrease sharply up to 2 km, followed by a descending stream with increasing entropy.

The isentropic-mean overturning circulation during the final 12 h of the spinup period is presented in Figs. 9b and 9d for both simulations. The moist simulation continues to have a deep overturning circulation, which is stronger than during the preconditioning period. The overturning circulation in the dry simulation has deepened with the greatest changes in the upper troposphere. The upward branch in both simulations has an increase in the low-level entropy compared to the preconditioning period, but the moist simulation still has a higher mean entropy. A strong, shallow overturning circulation persists during the spinup period.

To separate the locations of the deep and shallow overturning circulations, we look at the mean vertical mass flux and streamfunction in two regions during the

spinup period, the inner 300 km, and radii between 300 and 600 km. Figures 10a and 10c show the vertical mass flux and streamfunction in the inner 300 km during the spinup period (the preconditioning period has similar results). Both simulations have convection in the inner 300 km that is associated with domain-relative upward motion and entropy that decreases slightly with height, similar to Figs. 9b and 9d. The main difference in upward motion between simulations resides in the entropy at low levels. The moist and dry simulations have average entropy values of roughly 2635 and $2625 \text{ J kg}^{-1} \text{ K}^{-1}$ below 3 km, respectively. Thus, the mean entropy is lower for deep convection in the dry simulation. The main impact of dry air on convection does not appear to be entrainment directly into updrafts. Instead, differences are rooted in the subcloud layer, despite the simulations beginning with the same subcloud-layer entropy.

The isentropic vertical mass flux and streamfunction for radii between 300 and 600 km are shown in Figs. 10b and 10d. The shallow overturning circulation exists at these radii, outside the region of relatively frequent deep convection, and has the potential to transport low-entropy air into the subcloud layer. The moist simulation has an upward stream, beginning with entropy values between 2620 and $2630 \text{ J kg}^{-1} \text{ K}^{-1}$ that decrease with height, which reaches from 3 to 5 km. The downward stream starts at about 6 km with entropy values as

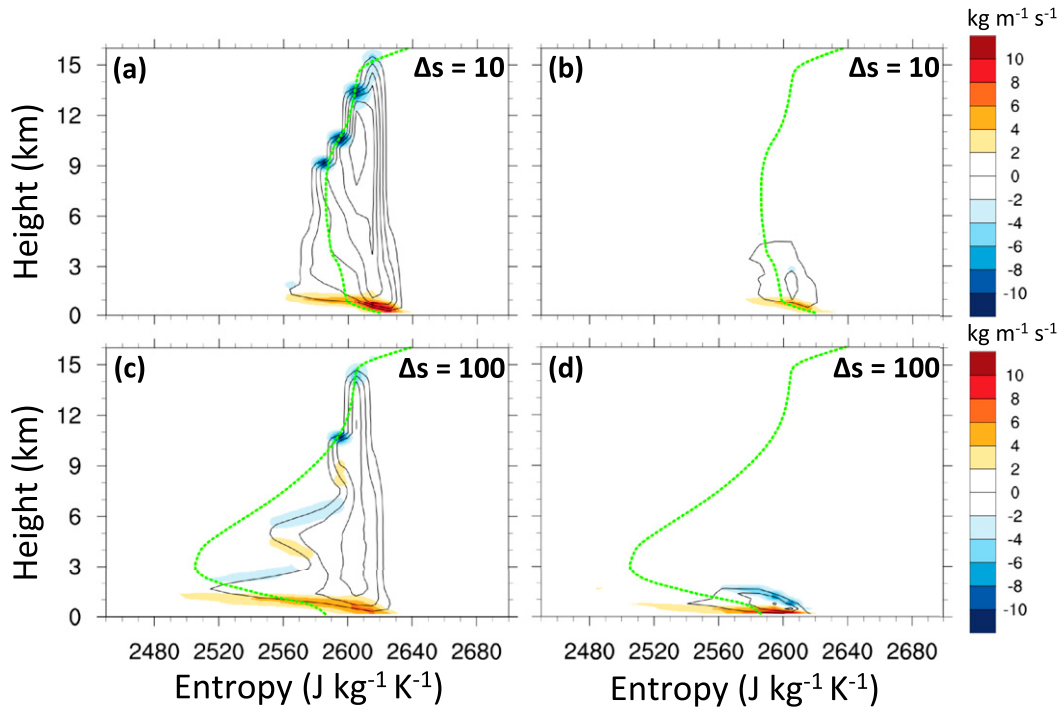


FIG. 11. Time-averaged, isentropic mass-weighted diabatic tendency (shaded, $\times 10^6 \text{ kg m}^{-1} \text{ s}^{-1}$) with an initial Δs of (a),(b) 10 and (c),(d) 100 $\text{J kg}^{-1} \text{ K}^{-1}$ for (a),(c) the inner 300 km and (b),(d) radii between 300 and 600 km. The streamfunction contours, green dotted line, and time average are as in Fig. 10.

low as $2570 \text{ J kg}^{-1} \text{ K}^{-1}$. In contrast, the dry simulation has a shallower overturning circulation, with the upward stream experiencing a quicker decrease in entropy with height. The downward stream starts at a height of about 2 km with moist entropy values as low as $2550 \text{ J kg}^{-1} \text{ K}^{-1}$. The shallow overturning circulations in both simulations mix higher-entropy air in the subcloud layer with lower-entropy air above the subcloud layer, with the dry simulation having lower-entropy air intruding into the subcloud layer between 300 and 600 km.

The entropy framework can also be used to calculate the mass-weighted diabatic tendency, which allows one to directly diagnose sources and sinks of entropy. Pauluis and Mrowiec (2013) derive the mass-weighted diabatic tendency from the continuity equation, given as

$$\langle \rho \dot{S} \rangle = -\frac{\partial \Psi}{\partial z}, \quad (8)$$

where $\langle \rho \dot{S} \rangle$ is the mass-weighted diabatic tendency. This equation is for a statistically steady state and is valid when the local time derivative of density is small compared to both terms in Eq. (8), which is true (not shown).

In the ASPECH model, the entropy of parcels can be changed in the following ways: 1) surface fluxes increase the entropy, 2) radiational cooling decreases the entropy,

and 3) turbulent mixing diffuses the entropy from high- to low-entropy streams. Low-entropy air at midlevels can affect convection through turbulent mixing into convective updrafts and/or the inflow layer. Calculating the mass-weighted diabatic tendency offers a way to determine the importance of these turbulent entrainment processes on the mean isentropic overturning circulation.

Figure 11 shows the mass-weighted diabatic tendency calculated from the isentropic streamfunction in Fig. 10. In the inner 300 km (Figs. 11a and 11c), the mass-weighted diabatic tendency is positive at low levels, associated with surface fluxes. As parcels rise within the upward branch in Fig. 10, the mass-weighted diabatic tendency is small, consistent with only a slight decrease in entropy. Turbulent mixing in the upward branch does not appear to be larger in the dry simulation. This result is consistent with the lack of lateral midlevel entrainment found in the 3D experiment in Riemer and Laliberté (2015).

The downward branch in the dry simulation has a wavy structure. We hypothesize that this pattern is due to radiational cooling, which has a negative diabatic tendency, and turbulent mixing between detraining convection and environmental air, which shows up as dipoles of positive and negative diabatic tendency at different levels. The positive pole occurs at lower

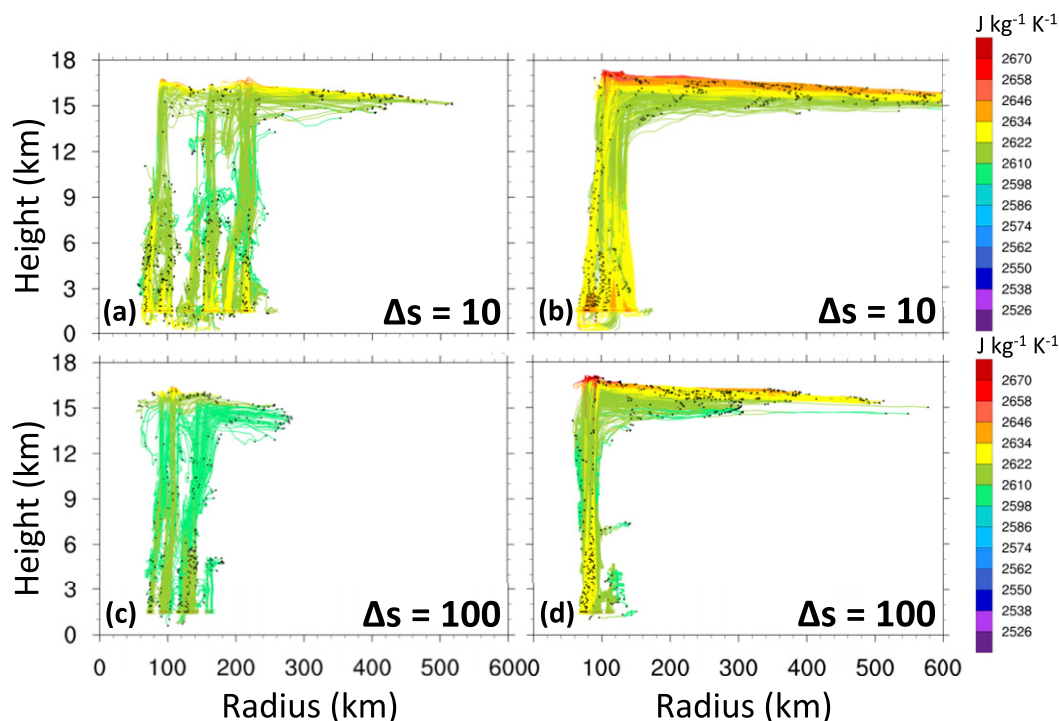


FIG. 12. Forward trajectories for a single run with an initial Δs of (a),(b) 10 and (c),(d) 100 J kg⁻¹ K⁻¹. The trajectories are tracked for the final 12 h of the (a),(c) preconditioning and (b),(d) spinup periods. Colors represent the entropy (J kg⁻¹ K⁻¹) of each trajectory. Solid black dots represent the final location of each trajectory.

entropy and the negative pole occurs at higher entropy and may be offset with height due to vertical mixing. Between 300 and 600 km (Figs. 11b and 11d), surface fluxes increase the entropy at low levels and turbulent mixing diffuses entropy from high- to low-entropy streams, especially in the dry simulation. This turbulent vertical mixing transports low-entropy air into the subcloud layer.

4. Trajectory analysis

The entropy framework suggests that midlevel low-entropy air only slightly impacts convective motions through turbulent mixing directly into deep convection. Instead, the analysis suggests that low-entropy air affects convection at its origin in the subcloud layer. Forward and backward trajectories are used to determine the influence of midlevel dry air on the entropy evolution of individual parcels within deep convection and the subcloud layer, respectively. Trajectories are initialized at a height of 1.5 km, near the top of the boundary layer, and within a radius of 300 km from the center. Only points at this height that have vertical velocity greater than 0.5 ms⁻¹ are tracked, representing convective updrafts. The 6-min model output is linearly interpolated to 1 min to increase the accuracy

of the trajectories. A Runge–Kutta fourth-order scheme is used to generate the trajectories, and additional trajectories are initialized every 6 min.

Figure 12 shows forward trajectories in the moist (Fig. 12a) and dry (Fig. 12c) simulations during the final 12 h of the preconditioning period. Likewise, Figs. 12b and 12d are for the final 12 h of the spinup period. The moist simulation has a larger radial width of upward motion and an outflow that extends to a larger radius compared to the dry simulation, consistent with Figs. 4 and 5. The moist simulation also has parcels with greater entropy. The entropy values are higher near the surface for both simulations and decrease by about 10 J kg⁻¹ K⁻¹ as the parcels rise, consistent with Fig. 9. Entrainment of low-entropy air from the environment into convection does not appear greater in the dry simulation, even though the dry simulation has lower entropy at midlevels adjacent to the convection. Still, the dry simulation has convective updrafts with a lower initial entropy as they rise out of the boundary layer, so entrainment may have a greater impact in reducing buoyancy and convective strength in the dry simulation.

Backward trajectories are used to diagnose the history of parcels before they rise in convective updrafts and to determine the source region of low-entropy air. Figures 13a and 13b show trajectories initialized at a

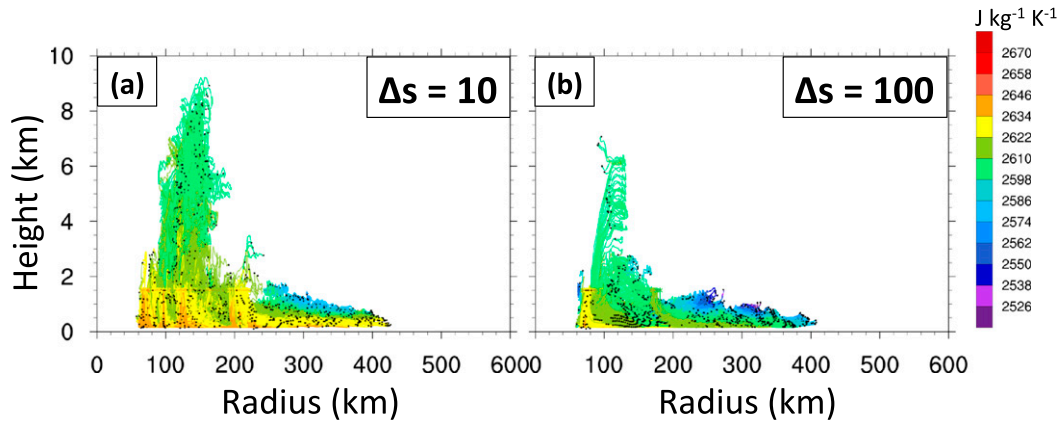


FIG. 13. Backward trajectories for a single run with an initial Δs of (a) 10 and (b) $100 \text{ J kg}^{-1} \text{ K}^{-1}$. The trajectories are tracked for the final 24 h of the spinup period. Colors represent the entropy ($\text{J kg}^{-1} \text{ K}^{-1}$) of each trajectory. Solid black dots represent the final location of each trajectory.

height of 1.5 km and within a radius of 300 km for the final 24 h of the spinup period. The preconditioning period has similar results (not shown). A longer time period is used compared to the forward trajectories in order for the entropy evolution of parcels in the inflow layer to be fully shown. The backward trajectories have two general sets in both simulations. The first set originates from a height greater than 1.5 km. These trajectories, which represent a small percentage of the total trajectories, pass through convective downdrafts and generally have a lower entropy than the convective updrafts in Figs. 12b and 12d. The second set has trajectories within the inflow layer. We focus on this set of trajectories to diagnose the effect of midlevel low-entropy air on parcels in the inflow layer.

Figure 14 shows the entropy and height evolution of the backward trajectories in the second set. The moist simulation has trajectories with high entropy (greater than $2622 \text{ J kg}^{-1} \text{ K}^{-1}$) outward of 100 km (Fig. 13a). The mean entropy of the trajectories in the moist simulation begins at about $2600 \text{ J kg}^{-1} \text{ K}^{-1}$ and slowly increases with time as the parcels move inward (Fig. 14a). While some of these trajectories originate from a height greater than 1 km, their minimum entropies do not fall below $2570 \text{ J kg}^{-1} \text{ K}^{-1}$. As parcels associated with these trajectories subside, their entropies increase at a faster rate than parcels that are always near the surface, owing to turbulent mixing and surface fluxes.

The dry simulation has trajectories with much lower entropy both outward of 100 km and closer to the TC center compared to the moist simulation (Fig. 13b). The mean entropy of the trajectories in the dry simulation begins at about $2580 \text{ J kg}^{-1} \text{ K}^{-1}$, $20 \text{ J kg}^{-1} \text{ K}^{-1}$ less than the moist simulation, and increases at a faster rate compared to the moist simulation as parcels move inward

(Fig. 14b). However, the range in entropy among the trajectories is larger for the dry simulation, particularly between -20 and -8 h. During this period, there are more trajectories originating from heights greater than 1 km with entropies less than $2580 \text{ J kg}^{-1} \text{ K}^{-1}$ compared to the moist simulation. There is, thus, a greater supply of subsiding low-entropy parcels closer in both time and space to the convective updrafts. Downward motion at radii closer to the TC center is confirmed in the Eulerian analysis (Figs. 6b and 6d) and the distribution of backward trajectories (Figs. 13a and 13b), and may be why deep convection is more radially confined.

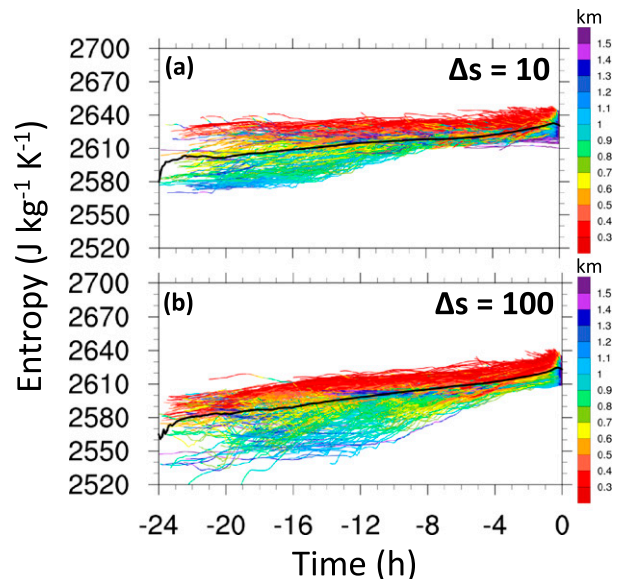


FIG. 14. Entropy time series of each backward trajectory in Figs. 13a and 13b with an initial Δs of (a) 10 and (b) $100 \text{ J kg}^{-1} \text{ K}^{-1}$. Colors represent the height of each trajectory at a given time. Only trajectories within the radial inflow layer are shown. The solid black line represents the mean entropy.

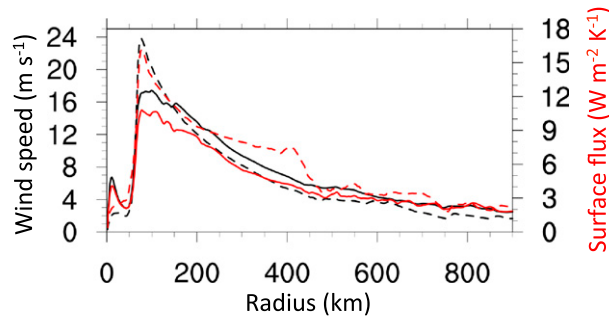


FIG. 15. Radial profiles of the 10-m wind (m s^{-1} , black) and surface fluxes ($\times 10 \text{ W m}^{-2} \text{ K}^{-1}$, red) with an initial Δs of 10 (solid) and $100 \text{ J kg}^{-1} \text{ K}^{-1}$ (dashed) averaged over the same 24 h of the backward trajectories.

Surface fluxes are examined to better understand the entropy evolution of parcels in the radial inflow layer. Figure 15 shows radial profiles of the 10-m wind speed and surface fluxes averaged during the same time period as the backward trajectories. In the moist simulation, the 10-m wind speed reaches 18 m s^{-1} at a radius of 100 km and gradually decreases with increasing radius. Surface fluxes follow the shape of the 10-m wind profile, indicating that the radial structure of surface fluxes is dominated by the wind speed over the air–sea disequilibrium. The dry simulation has a higher 10-m wind speed at a radius of 75 km that quickly decreases with increasing radius, resulting in a sharper radial profile (also shown in Fig. 3). The radial structure of surface fluxes is dominated by the wind speed inward of 150 km but then deviates from the 10-m wind profile between 150 and 450 km. This deviation must be due to larger air–sea disequilibrium enhancing the surface fluxes over this region, as low-entropy air descends into the inflow layer. The greater surface fluxes at these radii increase the entropy of parcels in the inflow layer at a quicker rate, but recovery takes longer owing to the lower initial entropy of parcels compared to the moist simulation (Fig. 14). Thus, the inflow trajectories in the dry experiment contribute to the decreased radial width of convection and, subsequently, the decreased size and strength of the secondary circulation.

5. Conclusions

The ASPECH model was used to assess the impact of midlevel low-entropy air on the development of the TC secondary circulation. This modeling framework conserves entropy in the absence of internal and boundary sources and sinks, allowing the thermodynamic characteristics of convective motions to be systematically tracked. A suite of experiments was conducted with different initial entropy deficits above the subcloud layer from a nearly saturated to a very dry free troposphere. The

evolution of the simulated TCs in the different moisture environments were compared during two phases: the preconditioning and spinup periods. Results showed that the moist simulation had a larger radial width of deep convection and a larger, stronger secondary circulation.

The Eulerian radius–height framework showed stronger convective motions in the moist simulation, but upward and downward motions occupy the same space. A Lagrangian framework separated high- and low-entropy streams from one another, allowing for a systematic accounting of the entropy evolution within convective parcels. In turn, this framework explicitly quantified lateral turbulent entrainment of low-entropy air directly into convective updrafts and vertical turbulent entrainment into the radial inflow layer. The vertical mass flux and mass-weighted diabatic tendency showed that turbulent entrainment of low-entropy air directly into deep convection slightly decreased the entropy in convective updrafts by roughly the same amount in the moist and dry simulations. However, the impact of entrainment on convection may have been more detrimental in the dry simulation since parcels began with a lower entropy.

A trajectory analysis was used to further determine how low-entropy air impacted convective motions and to determine the source region of low-entropy air. Forward trajectories of parcels in convective updrafts showed only a slight decrease in entropy from the surface to the upper troposphere in the moist and dry simulations. Backward trajectories showed that low- to midlevel low-entropy air subsided into the radial inflow layer, especially in the dry simulation. The parcel trajectories in the dry simulation had lower initial entropy and subsided closer in time and space to convective updrafts. Surface fluxes increased the entropy, but the recovery took longer in the dry simulation owing to the lower initial entropy. These factors likely contributed to the smaller and weaker secondary circulation.

This study has shown that low-entropy midlevel air affects the upward vertical mass flux in these experiments through subsidence into the subcloud layer, which results in a longer recovery time for entropy before deep convection develops. This process, as well as descending motion closer to the inner core, limits the radial width of deep convection, reduces the area of upward motion, and results in less total positive vertical mass flux (Tang et al. 2016). This study adds to previous work, describing the effects of boundary layer modification on changes in TC intensity, by showing that boundary layer modification also plays a role in the development of the secondary circulation.

Convective motions in TCs can be highly asymmetric in reality, limiting the extent to which these simulations represent reality. Processes such as asymmetric eddy

motions that drive midlevel entrainment, horizontal moisture gradients, and asymmetric convection cannot be represented in an axisymmetric modeling framework. Additionally, a simple warm-rain microphysics scheme was used in these simulations. The axisymmetric experiments are certainly not reality, but it is encouraging that the results are consistent with the 3D results of [Riemer and Laliberté \(2015\)](#). Additionally, recent 3D simulations conducted by the authors using a similar model setup as this study have shown comparable results that will be reported upon in a forthcoming manuscript. Future work will examine the hypotheses set forth in this study with the addition of vertical wind shear to assess the impact of dry midlevel air on lateral entrainment directly into convection and boundary layer modification, similar to [Riemer and Laliberté \(2015\)](#). Different initial vertical wind shear and moisture profiles will be used to assess the combined effects of dry air and vertical wind shear on the strength and structure of convection within the developing TC secondary circulation.

Acknowledgments. Thank you to David Raymond and two anonymous reviewers for their suggestions to improve the contents of this manuscript. Joshua Alland was funded by the National Science Foundation Graduate Research Fellowship Grant DGE 1060277.

REFERENCES

- Barnes, G. M., E. J. Zipser, D. Jorgensen, and F. Marks Jr., 1983: Mesoscale and convective structure of a hurricane rainband. *J. Atmos. Sci.*, **40**, 2125–2137, doi:[10.1175/1520-0469\(1983\)040<2125:MACSOA>2.0.CO;2](#).
- Bister, M., and K. A. Emanuel, 1997: The genesis of Hurricane Guillermo: TEXMEX analyses and a modeling study. *Mon. Wea. Rev.*, **125**, 2662–2682, doi:[10.1175/1520-0493\(1997\)125<2662:TGOHGT>2.0.CO;2](#).
- Black, P. G., and Coauthors, 2007: Air–sea exchange in hurricanes: Synthesis of observations from the Coupled Boundary Layer Air–Sea Transfer Experiment. *Bull. Amer. Meteor. Soc.*, **88**, 357–374, doi:[10.1175/BAMS-88-3-357](#).
- Braun, S. A., J. A. Sippel, and D. S. Nolan, 2012: The impact of dry midlevel air on hurricane intensity in idealized simulations with no mean flow. *J. Atmos. Sci.*, **69**, 236–257, doi:[10.1175/JAS-D-10-05007.1](#).
- Brown, R. G., and C. Zhang, 1997: Variability of midtropospheric moisture and its effect on cloud-top height distribution during TOGA COARE. *J. Atmos. Sci.*, **54**, 2760–2774, doi:[10.1175/1520-0469\(1997\)054<2760:VOMMAI>2.0.CO;2](#).
- Bryan, G. H., 2008: On the computation of pseudoadiabatic entropy and equivalent potential temperature. *Mon. Wea. Rev.*, **136**, 5239–5245, doi:[10.1175/2008MWR2593.1](#).
- Cram, T. A., J. Persing, M. T. Montgomery, and S. A. Braun, 2007: A Lagrangian trajectory view on transport and mixing processes between the eye, eyewall, and environment using a high-resolution simulation of Hurricane Bonnie (1998). *J. Atmos. Sci.*, **64**, 1835–1856, doi:[10.1175/JAS3921.1](#).
- Davis, C. A., and D. A. Ahijevych, 2012: Mesoscale structural evolution of three tropical weather systems observed during PREDICT. *J. Atmos. Sci.*, **69**, 1284–1305, doi:[10.1175/JAS-D-11-0225.1](#).
- Didlake, A. C., and R. A. Houze, 2009: Convective-scale downdrafts in the principal rainband of Hurricane Katrina (2005). *Mon. Wea. Rev.*, **137**, 3269–3293, doi:[10.1175/2009MWR2827.1](#).
- Donelan, M. A., B. K. Haus, N. Reul, W. J. Plant, M. Stiassnie, H. C. Graber, O. B. Brown, and E. S. Saltzman, 2004: On the limiting aerodynamic roughness of the ocean in very strong winds. *Geophys. Res. Lett.*, **31**, L18306, doi:[10.1029/2004GL019460](#).
- Dunion, J. P., 2011: Rewriting the climatology of the tropical North Atlantic and Caribbean Sea atmosphere. *J. Climate*, **24**, 893–908, doi:[10.1175/2010JCLI3496.1](#).
- Emanuel, K. A., 1989: The finite-amplitude nature of tropical cyclogenesis. *J. Atmos. Sci.*, **46**, 3431–3456, doi:[10.1175/1520-0469\(1989\)046<3431:TFANOT>2.0.CO;2](#).
- , 1995: The behavior of a simple hurricane model using a convective scheme based on subcloud-layer entropy equilibrium. *J. Atmos. Sci.*, **52**, 3960–3968, doi:[10.1175/1520-0469\(1995\)052<3960:TBOASH>2.0.CO;2](#).
- , 2010: Tropical cyclone activity downscaled from NOAA-CIRES reanalysis, 1908–1958. *J. Adv. Model. Earth Syst.*, **2**(1), doi:[10.3894/JAMES.2010.2.1](#).
- Emanuel, K., C. DesAutels, C. Holloway, and R. Korty, 2004: Environmental control of tropical cyclone intensity. *J. Atmos. Sci.*, **61**, 843–858, doi:[10.1175/1520-0469\(2004\)061<0843:ECOTCI>2.0.CO;2](#).
- , R. Sundararajan, and J. Williams, 2008: Hurricanes and global warming: Results from downscaling IPCC AR4 simulations. *Bull. Amer. Meteor. Soc.*, **89**, 347–367, doi:[10.1175/BAMS-89-3-347](#).
- Fairall, C. W., E. F. Bradley, D. P. Rogers, J. B. Edson, and G. S. Young, 1996: Bulk parameterization of air–sea fluxes for Tropical Ocean–Global Atmosphere Coupled–Ocean Atmosphere Response Experiment. *J. Geophys. Res.*, **101**, 3747–3764, doi:[10.1029/95JC03205](#).
- Frank, W. M., and E. A. Ritchie, 2001: Effects of vertical wind shear on the intensity and structure of numerically simulated hurricanes. *Mon. Wea. Rev.*, **129**, 2249–2269, doi:[10.1175/1520-0493\(2001\)129<2249:EOVWSO>2.0.CO;2](#).
- Ge, X., T. Li, and M. Peng, 2013: Effects of vertical shears and midlevel dry air on tropical cyclone developments. *J. Atmos. Sci.*, **70**, 3859–3875, doi:[10.1175/JAS-D-13-066.1](#).
- Haus, B. K., D. Jeong, M. A. Donelan, J. A. Zhang, and I. Savelyev, 2010: Relative rates of sea–air heat transfer and frictional drag in very high winds. *Geophys. Res. Lett.*, **37**, L07802, doi:[10.1029/2009GL042206](#).
- Hence, D. A., and R. A. Houze Jr., 2008: Kinematic structure of convective-scale elements in the rainbands of Hurricanes Katrina and Rita (2005). *J. Geophys. Res.*, **113**, D15108, doi:[10.1029/2007JD009429](#).
- Hill, K. A., and G. M. Lackmann, 2009: Influence of environmental humidity on tropical cyclone size. *Mon. Wea. Rev.*, **137**, 3294–3315, doi:[10.1175/2009MWR2679.1](#).
- James, R. P., and P. M. Markowski, 2010: A numerical investigation of the effects of dry air aloft on deep convection. *Mon. Wea. Rev.*, **138**, 140–161, doi:[10.1175/2009MWR3018.1](#).
- Jordan, C. L., 1958: Mean soundings for the West Indies area. *J. Meteor.*, **15**, 91–97, doi:[10.1175/1520-0469\(1958\)015<0091:MSFTWI>2.0.CO;2](#).
- Kessler, E., 1969: *On the Distribution and Continuity of Water Substance in Atmospheric Circulations*. Meteor. Monogr., No. 32, Amer. Meteor. Soc., 84 pp., doi:[10.1007/978-1-935704-36-2_1](#).

- Kimball, S. K., 2006: A modeling study of hurricane landfall in a dry environment. *Mon. Wea. Rev.*, **134**, 1901–1918, doi:10.1175/MWR3155.1.
- Knaff, J. A., C. R. Sampson, P. J. Fitzpatrick, Y. Jin, and C. M. Hill, 2011: Simple diagnosis of tropical cyclone structure via pressure gradients. *Wea. Forecasting*, **26**, 1020–1031, doi:10.1175/WAF-D-11-00013.1.
- Komaromi, W. A., 2013: An investigation of composite dropsonde profiles for developing and nondeveloping tropical waves during the 2010 PREDICT field campaign. *J. Atmos. Sci.*, **70**, 542–558, doi:10.1175/JAS-D-12-052.1.
- Matyas, C. J., and M. Cartaya, 2009: Comparing the rainfall patterns produced by Hurricanes Frances (2004) and Jeanne (2004) over Florida. *Southeast. Geogr.*, **49**, 132–156, doi:10.1353/sgo.0.0046.
- Molinari, J., J. Frank, and D. Vollaro, 2013: Convective bursts, downdraft cooling, and boundary layer recovery in a sheared tropical storm. *Mon. Wea. Rev.*, **141**, 1048–1060, doi:10.1175/MWR-D-12-00135.1.
- Mrowiec, A. A., O. M. Pauluis, and F. Zhang, 2016: Isentropic analysis of a simulated hurricane. *J. Atmos. Sci.*, **73**, 1857–1870, doi:10.1175/JAS-D-15-0063.1.
- Nolan, D. S., 2007: What is the trigger for tropical cyclogenesis? *Aust. Meteor. Mag.*, **56**, 241–266.
- , E. D. Rappin, and K. A. Emanuel, 2007: Tropical cyclogenesis sensitivity to environmental parameters in radiative-convective equilibrium. *Quart. J. Roy. Meteor. Soc.*, **133**, 2085–2107, doi:10.1002/qj.170.
- Ooyama, K., 1969: Numerical simulation of the life cycle of tropical cyclones. *J. Atmos. Sci.*, **26**, 3–40, doi:10.1175/1520-0469(1969)026<0003:NSOTLC>2.0.CO;2.
- Pauluis, O. M., and A. A. Mrowiec, 2013: Isentropic analysis of convective motions. *J. Atmos. Sci.*, **70**, 3673–3688, doi:10.1175/JAS-D-12-0205.1.
- , A. Czaja, and R. Korty, 2008: The global atmospheric circulation in moist isentropic coordinates. *Science*, **321**, 1075–1078, doi:10.1126/science.1159649.
- , —, and —, 2010: The global atmospheric circulation in moist isentropic coordinates. *J. Climate*, **23**, 3077–3093, doi:10.1175/2009JCLI2789.1.
- Powell, M. D., 1990: Boundary layer structure and dynamics in outer hurricane rainbands. Part II: Downdraft modification and mixed layer recovery. *Mon. Wea. Rev.*, **118**, 918–938, doi:10.1175/1520-0493(1990)118<0918:BLSADI>2.0.CO;2.
- Rappin, E. D., D. S. Nolan, and K. A. Emanuel, 2010: Thermodynamic control of tropical cyclogenesis in environments of radiative-convective equilibrium with shear. *Quart. J. Roy. Meteor. Soc.*, **136**, 1954–1971, doi:10.1002/qj.706.
- Raymond, D. J., 1995: Regulation of moist convection over the west Pacific warm pool. *J. Atmos. Sci.*, **52**, 3945–3959, doi:10.1175/1520-0469(1995)052<3945:ROMCOT>2.0.CO;2.
- , C. López-Carrillo, and L. L. Cavazos, 1998: Case-studies of developing east Pacific easterly waves. *Quart. J. Roy. Meteor. Soc.*, **124**, 2005–2034, doi:10.1002/qj.49712455011.
- , S. L. Sessions, and C. López Carrillo, 2011: Thermodynamics of tropical cyclogenesis in the northwest Pacific. *J. Geophys. Res.*, **116**, D18101, doi:10.1029/2011JD015624.
- Riemer, M., and F. Laliberté, 2015: Secondary circulation of tropical cyclones in vertical wind shear: Lagrangian diagnostic and pathways of environmental interaction. *J. Atmos. Sci.*, **72**, 3517–3536, doi:10.1175/JAS-D-14-0350.1.
- , M. T. Montgomery, and M. E. Nicholls, 2010: A new paradigm for intensity modification of tropical cyclones: Thermodynamic impact of vertical wind shear on the inflow layer. *Atmos. Chem. Phys.*, **10**, 3163–3188, doi:10.5194/acp-10-3163-2010.
- , —, and —, 2013: Further examination of the thermodynamic modification of the inflow layer of tropical cyclones by vertical wind shear. *Atmos. Chem. Phys.*, **13**, 327–346, doi:10.5194/acp-13-327-2013.
- Rios-Berrios, R., R. D. Torn, and C. A. Davis, 2016: An ensemble approach to investigate tropical cyclone intensification in sheared environments. Part II: Ophelia (2011). *J. Atmos. Sci.*, **73**, 1555–1575, doi:10.1175/JAS-D-15-0245.1.
- Rotunno, R., and K. A. Emanuel, 1987: An air–sea interaction theory for tropical cyclones. Part II: Evolutionary study using a non-hydrostatic axisymmetric numerical model. *J. Atmos. Sci.*, **44**, 542–561, doi:10.1175/1520-0469(1987)044<0542:AAITFT>2.0.CO;2.
- Shelton, K. L., and J. Molinari, 2009: Life of a six-hour hurricane. *Mon. Wea. Rev.*, **137**, 51–67, doi:10.1175/2008MWR2472.1.
- Simpson, R., and R. Riehl, 1958: Mid-tropospheric ventilation as a constraint on hurricane development and maintenance. Preprints, *First Technical Conf. on Hurricanes*, Miami Beach, FL, Amer. Meteor. Soc., D4-1–D4-10.
- Smith, R. K., 2006: Accurate determination of a balanced axisymmetric vortex in a compressible atmosphere. *Tellus*, **58A**, 98–103, doi:10.1111/j.1600-0870.2006.00149.x.
- , and M. T. Montgomery, 2012: Observations of the convective environment in developing and non-developing tropical disturbances. *Quart. J. Roy. Meteor. Soc.*, **138**, 1721–1739, doi:10.1002/qj.1910.
- Tang, B., and K. Emanuel, 2010: Midlevel ventilations constraint on tropical cyclone intensity. *J. Atmos. Sci.*, **67**, 1817–1830, doi:10.1175/2010JAS3318.1.
- , and —, 2012a: Sensitivity of tropical cyclone intensity to ventilation in an axisymmetric model. *J. Atmos. Sci.*, **69**, 2394–2413, doi:10.1175/JAS-D-11-0232.1.
- , and —, 2012b: A ventilation index for tropical cyclones. *Bull. Amer. Meteor. Soc.*, **93**, 1901–1912, doi:10.1175/BAMS-D-11-00165.1.
- , R. Rios-Berrios, J. J. Alland, J. D. Berman, and K. L. Corbosiero, 2016: Sensitivity of axisymmetric tropical cyclone spinup time to dry air aloft. *J. Atmos. Sci.*, **73**, 4269–4287, doi:10.1175/JAS-D-16-0068.1.
- Van Sang, N., R. K. Smith, and M. T. Montgomery, 2008: Tropical cyclone intensification and predictability in three dimensions. *Quart. J. Roy. Meteor. Soc.*, **134**, 563–582, doi:10.1002/qj.235.
- Wang, Y., 2009: How do outer spiral rainbands affect tropical cyclone structure and intensity? *J. Atmos. Sci.*, **66**, 1250–1273, doi:10.1175/2008JAS2737.1.
- Wang, Z., 2012: Thermodynamic aspects of tropical cyclone formation. *J. Atmos. Sci.*, **69**, 2433–2451, doi:10.1175/JAS-D-11-0298.1.
- , 2014: Role of cumulus congestus in tropical cyclone formation in a high-resolution numerical model simulation. *J. Atmos. Sci.*, **71**, 1681–1700, doi:10.1175/JAS-D-13-0257.1.
- Xu, J., and Y. Wang, 2010: Sensitivity of the simulated tropical cyclone inner-core size to the initial vortex size. *Mon. Wea. Rev.*, **138**, 4135–4157, doi:10.1175/2010MWR3335.1.
- Ying, Y., and Q. Zhang, 2012: A modeling study on tropical cyclone structural changes in response to ambient moisture variations. *J. Meteor. Soc. Japan*, **90**, 755–770, doi:10.2151/jmsj.2012-512.
- Zawislak, J., and E. J. Zipser, 2014: Analysis of the thermodynamic properties of developing and nondeveloping tropical disturbances using a comprehensive dropsonde dataset. *Mon. Wea. Rev.*, **142**, 1250–1264, doi:10.1175/MWR-D-13-00253.1.